nature structural & molecular biology

Copper-transporting P-type ATPases use a unique ion-release pathway

Magnus Andersson[1,4,5], Daniel Mattle[2,4,5], Oleg Sitsel[2], Tetyana Klymchuk[2], Anna Marie Nielsen[2], Lisbeth Birk Møller[3], Stephen H White[1], Poul Nissen[2] & Pontus Gourdon[2]

Heavy metals in cells are typically regulated by P_{IB}-type ATPases. The first structure of the class, a Cu^+-ATPase from *Legionella pneumophila* (LpCopA), outlined a copper transport pathway across the membrane, which was inferred to be occluded. Here we show by molecular dynamics simulations that extracellular water solvated the transmembrane (TM) domain, results indicative of a Cu^+-release pathway. Furthermore, a new LpCopA crystal structure determined at 2.8-Å resolution, trapped in the preceding E2P state, delineated the same passage, and site-directed-mutagenesis activity assays support a functional role for the conduit. The structural similarities between the TM domains of the two conformations suggest that Cu^+-ATPases couple dephosphorylation and ion extrusion differently than do the well-characterized P_{II}-type ATPases. The ion pathway explains why certain Menkes' and Wilson's disease mutations impair protein function and points to a site for inhibitors targeting pathogens.

Class IB P-type ATPases (P_{IB}-type ATPases) that perform active transport of heavy metals across cellular membranes are of crucial importance for heavy-metal homeostasis[1–3]. The Cu^+-ATPase subclass (CopA), the most widespread among P_{IB}-type ATPases, has attracted particular attention because malfunction of the human members ATP7A and ATP7B is the direct cause of the severe Menkes' and Wilson's diseases, respectively[4,5]. To understand the under lying mechanisms of heavy-metal transport and disease, the transport pathway and its coupling to the ATPase reaction cycle must be described. The mechanistic view of how P-type ATPases mediate ion flux across the membrane has emerged primarily from studies of P_{II}-type ATPases, such as the sarco(endo)plasmic reticulum Ca^{2+}-ATPase (SERCA)[6–15] (**Fig. 1a**). The E1 state binds intracellular ions with high affinity, and then occlusion and phosphorylation (forming the E1P state) trigger conformational changes and access to the extracellular (luminal) environment (forming the E2P state). The ions are then released, and extracellular (luminal) counterions (protons for SERCA) bind and stimulate reocclusion and dephosphorylation (during which the E2.P_i transition state is formed; P_i, inorganic phosphate). Release of bound phosphate yields the fully dephosphorylated conformation (E2), which then shifts into the inward-facing conformation (E1) to initiate a new reaction cycle. As a result, SERCA transports two calcium ions and countertransports two to three protons, and this is accompanied by ATP turnover and structural rearrangements[16]. However, it is not clear whether a similar E1↔E2 reaction scheme applies to other classes of P-type ATPases, particularly those for which countertransport may not apply, such as the P_{IB}-type ATPases[17].

Recently, the structure of a Cu^+-exporting P_{IB}-type ATPase from *L. pneumophila* (LpCopA) was determined in a Cu^+-free transition state of dephosphorylation (E2.P_i), as mimicked by addition of AlF_4^- (PDB 3RFU[18]). The structure demonstrated a preserved P-type ATPase core structure with intracellular actuator (A), phosphorylation (P) and nucleotide-binding (N) domains and a TM domain. Thus, the regions responsible for phosphorylation and dephosphorylation in CopA are similar to those of SERCA. Moreover, putative Cu^+ sites of intracellular entry at Met148 (LpCopA numbering), internal coordination (involving the 382-Cys-Pro-Cys-384 motif) and extracellular exit (at Glu189) suggested a three-stage transport pathway across the TM domain that would be sensitive to conformational changes similar to those observed for P_{II}-type ATPases[18]. However, the intramembranous ion-binding cluster of CopA[19] lacks carboxylate residues, whereas in SERCA the equivalent region encompasses several negatively charged residues that participate in both calcium transport and H^+ countertransport[8–13,16]. Furthermore, the CopA topology is considerably different from that of the P_{II}-type ATPases: it contains P_{IB}-specific helices MA and MB and lacks helices M7 through M10 (**Fig. 1b**). Thus, it is possible that Cu^+ transport operates through a unique and class-specific mechanism. Here, to characterize CopA-mediated ion transport, we used a multidisciplinary approach combining molecular dynamics (MD) simulations, X-ray crystallography and mutational studies *in vitro* and *in vivo*. We determined an LpCopA crystal structure of the state associated with extracellular release in SERCA: the E2P conformation preceding E2.P_i in the forward direction of the reaction cycle (**Fig. 1a**). The observed structural similarity

[1]Department of Physiology and Biophysics, University of California at Irvine, Irvine, California, USA. [2]Centre for Membrane Pumps in Cells and Disease (PUMPkin), Danish National Research Foundation, Department of Molecular Biology and Genetics, Aarhus University, Aarhus, Denmark. [3]Applied Human Molecular Genetics, Kennedy Center, Copenhagen University Hospital, Rigshospitalet, Glostrup, Denmark. [4]Present addresses: Science for Life Laboratory, Theoretical and Computational Biophysics, Department of Theoretical Physics, Swedish e-Science Research Center, Royal Institute of Technology (KTH), Solna, Sweden (M.A.) and Laboratory of Biomolecular Research, Paul Scherrer Institut, Villigen, Switzerland (D.M.). [5]These authors contributed equally to this work. Correspondence should be addressed to P.G. (pgo@mb.au.dk).

Received 23 May; accepted 11 October; published online 8 December 2013; doi:10.1038/nsmb.2721

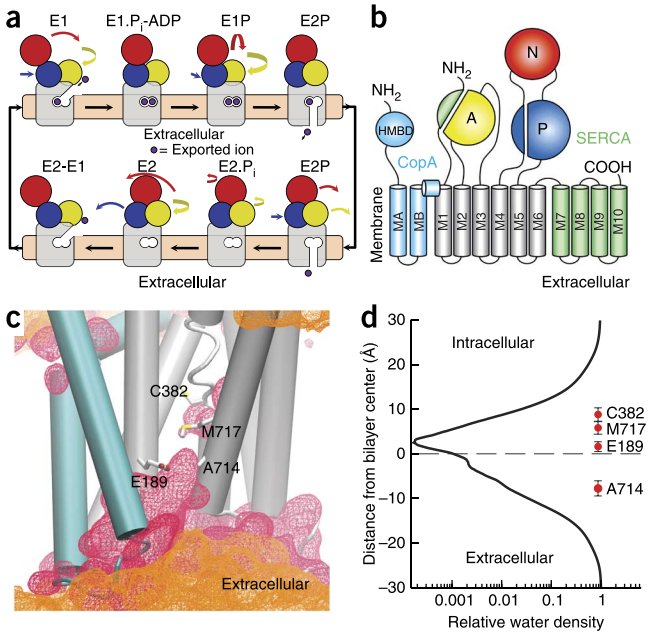

Figure 1 MD simulations suggest the E2.P$_i$ state to be open in CopA. (**a**) Schematics of the classical P-type–ATPase reaction cycle, known, for example, for Ca^{2+}-transporting SERCA. The intracellular A, P and N domains are colored yellow, blue and red, respectively, and the M domain is gray. Ions are shown in purple, and arrows indicate structural rearrangements. E2-E1 denotes transition between states. (**b**) Features unique to CopA (HMBD-MA-MB, cyan) and SERCA (A domain, N terminus and M7–M10 in green). (**c**) Average representation from the simulation of the CopA E2.P$_i$ state (PDB 3RFU[18]). The transmembrane domain is shown with helices MA and MB (class IB specific) and M1–M6 depicted as in **b**. Functionally relevant residues are shown as sticks. Lipid phosphates and water are shown as orange and red density surfaces at 5% and 20% occupancies, respectively (the fraction of presence in simulation frames). (**d**) Density plot for the water distribution of the E2.P$_i$ MD simulation showing the number of water molecules within 7 Å from the protein relative to bulk solution along the membrane normal (intracellular side is positive). The centers of mass with corresponding error bars are depicted for Cys382, Met717, Glu189 and Ala714. Error bars, s.d. (n = 100,000).

between the two LpCopA TM domains indicates that CopA couples the dephosphorylation event and occlusion of the TM domain differently than do the P_{II}-type ATPases, for which this state is associated with closure of the extracellular pathway. The MD simulations and crystal structure showed overlapping water molecules that indicate that the TM domains of the E2.P$_i$ and E2P states are both open toward the extracellular side, thus suggesting a class-specific ion-release pathway originating from ion-binding residues deep within the TM domain. These results may also explain why multiple Menkes' and Wilson's disease mutations are found in the equivalent regions of the human ATP7A and ATP7B transporters.

RESULTS

MD simulations suggest the E2.P$_i$ state to be open

By means of an MD simulation of the LpCopA E2.P$_i$ structure embedded in a dioleoylphosphocholine (DOPC) lipid bilayer, we searched the TM domain for pathways that link suggested areas of Cu^+ entry, intramembranous binding and exit. We surprisingly observed extracellular bulk water entering the TM domain and solvating the putative exit-site region at Glu189, occasionally reaching as far as the intramembranous copper-binding residues Cys382, Cys384 and Met717 (**Fig. 1c**,**d** and **Supplementary Movie 1**). The open E2.P$_i$ state hints at a class-specific release mechanism distinct from the one observed for SERCA, in which the corresponding state is closed (**Fig. 1a**). As for Ca^{2+} release in SERCA, Cu^+ must pass more than half of the membrane from the intramembranous ion-binding residues Cys382 and Met717 to be released to the extracellular side. However, the LpCopA extrusion pathway, involving TM helices M2 (with Glu189), M6 and the P_{IB}-specific N-terminal MA (**Fig. 1b**)[2], appears to be unique.

Crystal structure of the E2P state

The results of the MD simulation led us to crystallize LpCopA in a copper-free E2P state, using the phosphate analog BeF_3^-, which in SERCA yields the phosphoenzyme state that exposes the extracellular (luminal) release pathway[13]. The structure, determined at 2.8-Å resolution (**Fig. 2** and **Table 1**), revealed a similar configuration of the intracellular domains as for the corresponding E2P conformation of SERCA (**Fig. 2b** and **Supplementary Fig. 1a**). The TGE loop of the A domain interacts with the phosphorylated Asp426 (mimicked by BeF_3^- binding, **Supplementary Fig. 1b–e**) but is not primed for dephosphorylation. However, in contrast to SERCA, in which the E2P-to-E2.P$_i$ transition is accompanied by structural changes of TM helices M1 and M2, and M3 and M4 relative to the M5–M10 bundle that occludes protons from the extracellular side in the structure (r.m.s. deviation$_{backbone}$ 1.7 Å, **Fig. 3a**), the TM domain of LpCopA remained almost unchanged in the shift from E2P to E2.P$_i$ (r.m.s. deviation$_{backbone}$ 0.6 Å, **Fig. 3b**). Furthermore, two independent E2P crystal forms yielded similar crystal structures, so the structural differences between SERCA and LpCopA are not likely to be due to crystal-packing effects (**Supplementary Fig. 2** and **Table 1**).

The pathway coincided in the structures and simulations

Interestingly, multiple crystal waters in the new E2P structure delin eated a pathway (**Fig. 2a**,**c**), flanked by transmembrane helices MA, M2 and M6, that coincided with the hydration patterns derived from the MD simulation of the E2.P$_i$ structure. This extracellular water cleft was also reproduced in an MD simulation of the E2P structure (**Figs. 3c** and **4a** and **Supplementary Movies 1** and **2**), in which bulk water established a link between the putative exit site at Glu189 and the extracellular environment. Our combined simulation and crystallographic data therefore indicate the E2.P$_i$ and E2P conformations of LpCopA to be equally open toward the extracellular side with water reaching the internal ion-binding sites deep in the TM domain. At the same time, the protein remained closed toward the intracellular side, as required for an alternating access mechanism[20].

We then asked whether the observed water-filled pathway could accommodate Cu^+ ions, which is a prerequisite for ion transport. We calculated an outline of the pore radii in LpCopA from the Cys382, Cys384 and Met717 high-affinity ion-binding cluster to the extra cellular side, using CAVER[21]. Indeed, both crystal structures as well as average structures from the simulations reported pathway dimensions compatible with passage of Cu^+ ions[22] (**Fig. 3d** and **Supplementary Fig. 3h**,**i**). To enable a comparison to the LpCopA crystal structures, we stripped hydrogens from average structures from the simulations. Even so, the release-pathway radius in the simulated hydrogenated average structures was wider than was the Cu^+ ion radius. Similarly, analyses of the pore radii of the corresponding E2.P$_i$ (PDB 3B9R[13]) and E2P (PDB 3B9B[13]) SERCA states (without hydrogens), with the origin set close to the internal ion-binding sites defined by Ile307, Glu309 and Leu797, displayed an open E2P state in agreement with ion extrusion (**Fig. 3d**), whereas we found no pores for the E2.P$_i$ state, results in accordance with a proton-occluded state.

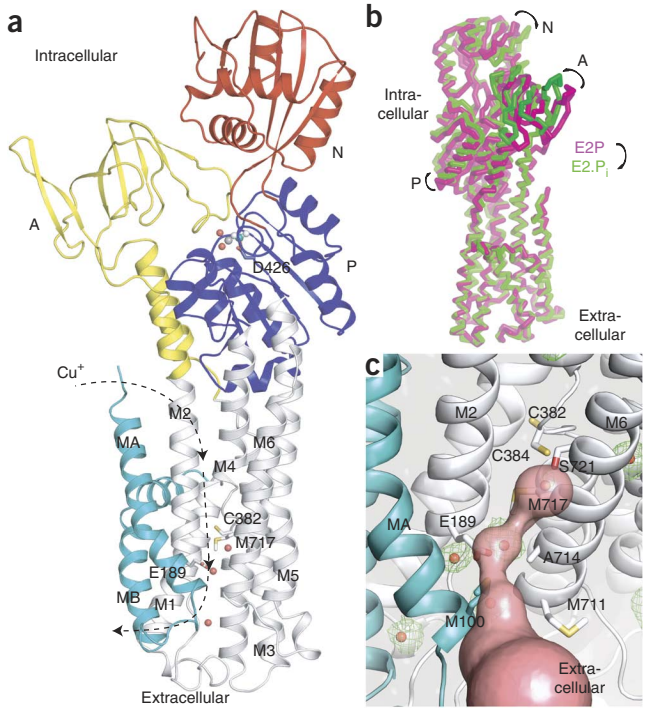

Figure 2 Crystal waters of the E2–BeF_3^- structure support the copper-release pathway. The domains are colored as in **Figure 1b**. (**a**) The E2–BeF_3^- structure determined in this work. Black arrows mark the direction of Cu^+ transport. Crystal waters located in close vicinity to Cys382, Met717 and Glu189 are shown as red spheres. (**b**) Superimpositions of the TM domains of the E2P (purple) and E2.P_i (green) states of LpCopA. Intracellular domains change their configuration from the E2P to the E2.P_i state (black arrows) while the TM domains remain rigid. (**c**) Close-up view of the extrusion pathway with residual $F_o - F_c$ electron density (green mesh at 2.5 σ, before modeling) of BeF_3^--bound LpCopA, with key residues labeled. The opening from the high-affinity Cu^+-coordinating residues Cys382, Cys384 and Met717 in the E2P conformation is displayed as a red surface, as obtained with CAVER[21], and overlays with crystallographic water molecules as red spheres.

The identified conduit allows for transfer of Cu^+

We observed pronounced side chain dynamics of Met717 and Glu189 that could be attributed to a possible role in shuttling of Cu^+ ions from the internal binding residues via the exit site to the extracellular compartment (**Fig. 4a**). To investigate the role of Met717 and Glu189 and the energetics involved in ion passage, we positioned a Cu^+ ion between the intramembranous high-affinity ligands Cys382 and Met717 and simulated its release. Even though the force applied on the ion was strictly perpendicular to the membrane, the ion followed our proposed release pathway, involving a 10-Å traverse movement in the membrane plane (**Fig. 5**). Met717 shuttled Cu^+ to Glu189, which then released the ion to the water-filled extracellular cavity. We detected no major energy barriers along the pathway, and the passage between Met717 and Glu189 was associated with favorable energetics (**Fig. 5**).

An intramembranous Cu^+ site

Comparison of the crystal structure and MD simulations revealed additional details of the exit pathway, including preferred locations for water molecules. Two crystallographic water molecules were located adjacent to critical residues implicated in high-affinity copper binding[19] and contributed to water pockets that were continuously occupied in the E2P simulation. Importantly, water pockets were also present at similar locations in the E2.P_i simulation. Even though water molecules associated with the release pathway in the E2.P_i simulation displayed high exchange rates, as defined by short residence times (<20 ps, **Fig. 4a** and **Supplementary Fig. 3f,g**), the water pockets remained occupied throughout the simulation. Crystal waters and simulated water dynamics have been used previously to probe ion-binding sites[23,24], and, remarkably, the internal water pockets in the simulations correspond by structural alignment to calcium site I of the occluded Ca_2-bound E1P conformation of SERCA (**Fig. 4a**). Therefore, the internal water pockets hint at a role of this site in copper transport.

Residues along the ion conduit are critical for function

To further validate the proposed ion conduit and mechanisms involved in ion release, we performed *in vitro* activity measurements of CopA point mutants, using a well-established ATPase assay[25] (**Fig. 4c**, **Supplementary Fig. 4a** and **Supplementary Table 1**). This assay showed Met717 to be crucial for function and identified both side chain size and charge to be important at position Glu189, which in the human copper pumps is conserved as an aspartate. The substantially reduced activity for the A714T mutation can be explained by direct steric hindrance of the observed pathway. Furthermore, although Met100 and Met711 both are positioned at the proposed exit site, only Met711 displays mutational sensitivity, results consistent with the peripheral locations of Met100 and M711 relative to the pathway, with Met100 being the most distant (**Fig. 4b**). All considered, the release pathway is supported by mutational effects, as probed by the ATPase activity, and provides a possible structural basis for the impaired copper-transport function resulting from previously perplexing missense mutations associated with Menkes' and Wilson's diseases, which are located in the vicinity of the extracellular

Table 1 Data collection and refinement statistics

	High-resolution structure	Low-resolution structure
Data collection		
Space group	*C*2	$P2_12_12_1$
Cell dimensions		
a, *b*, *c* (Å)	242.0, 71.4, 72.4	73.0, 85.0, 342.4
α, β, γ (°)	90, 100.01, 90	90, 90, 90
Resolution (Å)	48.2–2.7 (2.8–2.7)	85.6–7.11 (7.3–7.11)
R_{merge}	12.3 (96.7)	27.8 (125.6)
$I / \sigma I$	21.3 (2.0)	7.9 (3.5)
Completeness (%)	96.6 (94.1)	98.7 (99.6)
Redundancy	7 (7.2)	12.5 (12.2)
Refinement		
Resolution (Å)	48.2–2.75	85.6–7.1
No. reflections	30,867	3,468
R_{work} / R_{free}	0.199 / 0.247	0.305 / 0.333
No. atoms		
Protein	4,945	9,890
Ligand/ion	92	2
Water	59	
B factors		
Protein	66.4	
Ligand/ion	116.1	
Water	53.8	
r.m.s. deviations		
Bond lengths (Å)	0.010	
Bond angles (°)	1.23	

Outer-shell statistics are in parentheses. The structures are based on a single crystal each.

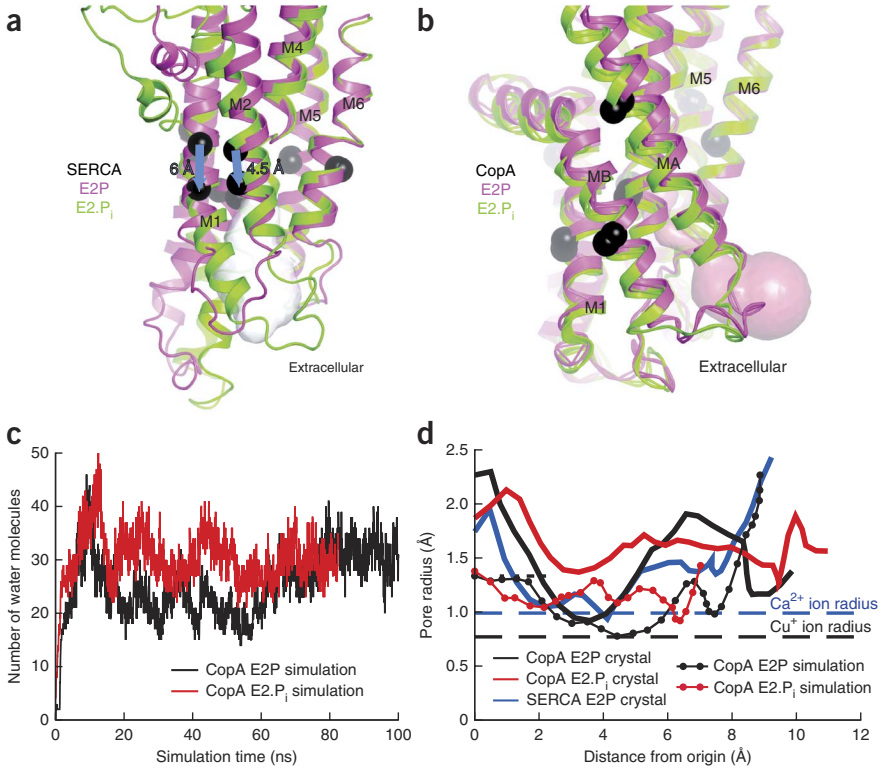

Figure 3 The CopA release pathway is unique and able to accommodate Cu^+ ions. (**a**) View of the transmembrane domains of the E2P (PDB 3B9B[13], purple) and E2.P_i (PDB 3B9R[13], green) structures of SERCA and its release pathway (white). Black spheres indicate the movements of one Cα atom in each helix, and transmembrane helices M7–M10 have been removed for clarity. Pronounced shifts of helices M1 and M2, and M3 and M4 relative to M5 and M6 occlude SERCA between E2P and E2.P_i. (**b**) Equivalent view as in **a** for CopA with its release pathway (purple), showing that CopA remains rigid in the E2P-to-E2.P_i (PDB 3RFU[18]) transition. (**c**) Number of water molecules associated with the release pathway in the E2P and E2.P_i simulations. (**d**) LpCopA pore radii of the E2P (black) and E2.P_i (red) crystal structures (straight lines) and average structures from the last 10 ns of the corresponding simulations (dotted lines) compared to the size of Cu^+ (black) and Ca^{2+} (blue). The corresponding radius in the E2P crystal structure of SERCA (PDB 3B9B[13]) is shown in blue. No pore was found in the SERCA E2.P_i state (PDB 3B9R[13]). The cutoff value for all analyses was set at a pore radius of 2.5 Å.

cleft lined by MA, M2 and M6 (refs. 18,26) (**Fig. 4d**). Consistently with our findings, the extracellular loop connecting MA and MB has been implicated in copper discharge in the human copper pump ATP7A[27].

Conserved prolines may control Cu^+ release

By tracking interhelical distances in the TM domain by means of Cα-to-Cα distances between helices MA and M6, M1 and M4, and M4 and M5 in the E2.P_i MD simulation, we observed a shift of 3–5 Å of the extracellular ends of TM helices MA and M6 (**Fig. 4b** and **Supplementary Fig. 5a**,**b**). This structural rearrangement originated from the well-conserved Pro94 and Pro710, thus suggesting a possible role for these residues in the opening of the release pathway to the exit site at Glu189. Moreover, the CAVER analyses showed average structures from the MD simulations to be more opened toward the extracellular side as compared to the corresponding crystal structures, results consistent with the observed shifts of the extracellular ends of TM helices MA and M6 (**Fig. 3d**).

In agreement with a proline-dependent opening mechanism, the *in vitro* assay reported impaired CopA activity for the P94A and P710A mutations (**Fig. 4c** and **Supplementary Table 1**). Moreover, two separate MD simulations of the proline mutants showed markedly distorted hydration patterns compared to those of wild type, thus providing a possible structural explanation for the observed phenotypes (**Supplementary Fig. 5f**,**g**). CAVER results on average structures from the mutant simulations predicted a misdirected pathway for the P94A mutant (**Supplementary Fig. 5c–e**,**f**). In the P710A simulation, the pathway from Glu189 was largely maintained, but the release

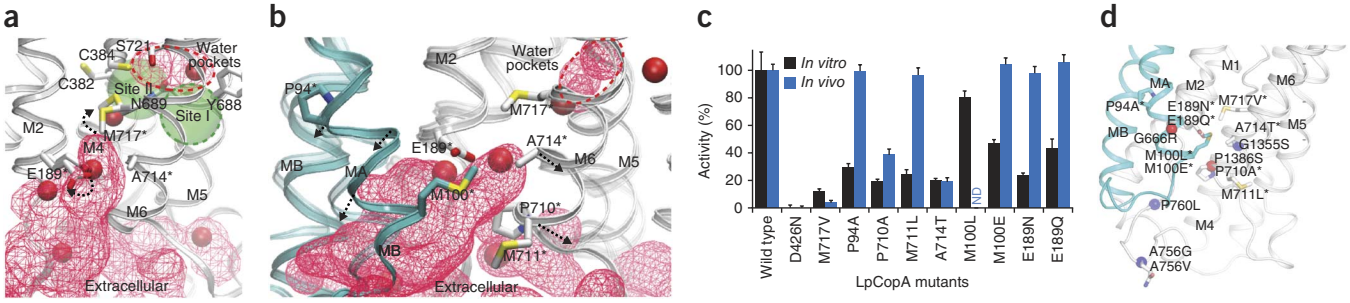

Figure 4 Copper transfer from the high-affinity binding sites and the extracellular release pathway. (**a**,**b**) Hydration and side chain dynamics of the LpCopA crystal structures, colored as in **Figure 1b** and with E2P crystal waters (solid red spheres). Asterisks mark residues included in the functional analysis summarized in **c**. Water pockets in the ion-binding region are encircled in red. (**a**) The E2P-state simulation. Crystallographic and simulated (averaged over the last 20 ns) side chain configurations are shown for Met717 and Glu189, and the E2P crystal structure represents Cys382, Cys384, Tyr688, Asn689, Ala714 and Ser721 because they do not rearrange extensively during simulations. Green, transparent spheres represent the approximate locations of the SERCA calcium sites (PDB 3BA6[13]). (**b**) An average from the last 20 ns of the E2.P_i simulation (transparent) superimposed on the E2.P_i (PDB 3RFU[18]) structure (solid). Arrows show movements of Cα atoms in MA and M6. (**c**) Relative *in vitro* (black) and *in vivo* (blue) activity of LpCopA copper-release-pathway mutants compared to wild-type protein and the inactive D426N mutant (black). ND, not determined. Error bars, technical s.d. ($n = 9$) for the *in vitro* data and biological s.d. ($n = 3$) for the *in vivo* data. (**d**) Missense mutations causing Menkes' (red spheres) and Wilson's (blue spheres) disease, located in the in extrusion-pathway region, plotted on the new E2P structure of LpCopA. Asterisks as in **a**.

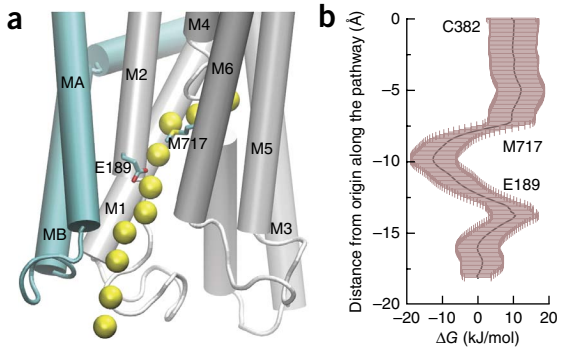

Figure 5 Energy barriers associated with the release pathway. (**a**) The release pathway as sampled by application of a force to a Cu^+ ion initially placed in the suggested ion-binding site at $z = 0$ Å, displayed by snapshots of the ion during the steered MD simulation (yellow spheres). Transmembrane helices are colored as in **Figure 1b**. (**b**) The accompanying potential of mean force profile, with the uncertainty given by the s.d. of 100 bootstrapped PMF profiles[38].

pathway and water pockets at the intramembranous ion-binding li gands contained a larger amount of water compared to that of the wild-type simulation (**Supplementary Fig. 5c–e,g**). Together, the *in vitro* data and accompanying MD simulations support Pro710 and Pro94 as key players for pore opening and ion release. Thus, whereas the intracellular segment of helix MB appears critical for copper uptake[18], an ion-extrusion function can be attributed to the extracellular part of MA (including Pro94), which is well conserved in Cu^+-ATPases (**Supplementary Fig. 6a**).

The exit pathway is physiologically relevant

To investigate the physiological significance of the proposed release pathway and mutations, we assessed the CopA mutations *in vivo* by LpCopA complementation of a CopA-deficient *Escherichia coli* strain, using LpCopA constructs controlled by the CopA promoter of the host (**Fig. 4c** and **Supplementary Fig. 4b,c**). A possible caveat with this approach is that extracellular Cu^+-accepting partners may be missing or incapable of recognizing the recombinant ATPase. However, because the D426N dead mutant (with no phosphoryl ation site) and wild-type LpCopA switched the copper tolerance of the *E. coli* strain, it was possible to use the assay as a proxy for functional Cu^+ transport *in vivo*. Overall, the general trends from ATPase activities *in vitro* were reproduced *in vivo*, albeit less pronouncedly (**Fig. 4c**). Strikingly, the two most potent *in vitro* mutations of the region, A714T (sterical block of the conduit) and P710A (opening to the extracellular compartment), also conferred a remarkable susceptibility to copper *in vivo*, thus substantiating the relevance of the release pathway for CopA copper transport in cells.

DISCUSSION

The combined results from our experiments and simulations map a putative release pathway in Cu^+-transporting P_{IB}-type ATPases, which appears to be available both in the E2P and E2.P_i states. The structural boundaries and chemical characteristics of this pathway, as well as the actual release mechanism, seem to be unique for the subclass. By ana logy to SERCA[16], the CopA transport mechanism might also involve counterions such as protons. However, so far, counterion require-ments have not been observed for any P_{IB}-type ATPase, and currents observed for the human copper transporter ATP7B are not sensitive to pH[28,29]. The unexpected open configuration of the E2.P_i structure also disfavors coupled countertransport of, for example, protons, for which occlusion of the TM domain would be expected (**Fig. 6**). Further supporting a distinctly tuned reaction cycle for Cu^+-ATPases, the ATP-induced phosphoenzyme formation has been observed in the absence and in the presence of the transported ion, unlike results for SERCA[30]. The unique features accompanying P_{IB}-type ATPase function can be explained in terms of substantial structural differences between P_{II}- and P_{IB}-type ATPases. For instance, the A domain–M1 linker that controls the Ca^{2+}-entry region in P_{II}-type ATPases is lacking in CopA. Because the A domain has a key role in transmitting conformational changes in the intracellular domains to changes in the TM domain, the missing linker might therefore offer a structural explanation to the differently tuned coupling between dephosphory lation and TM occlusion. The presence of the two additional TM helices MA and MB in CopA may also explain why their main interac tion partners, M1 and M2, are prevented from undergoing the major structural rearrangements observed in SERCA. Furthermore, CopA lacks the M7–M10 bundle, which in P_{II}-type ATPases (SERCA and Na^+,K^+-ATPase) contains a solvated channel in the E2 and E2.P_i states that presumably supports proton exchange[31] (**Fig. 1b**). This mechanistic differentiation may also apply within the P_{IB}-type ATPase subclasses; the MA helix in Zn^{2+}- and Co^{2+}-ATPases is lacking the corresponding Pro94, and the extracellular portion is less conserved compared to that of Cu^+-ATPases (**Supplementary Fig. 6**). Notably, distinct mechanisms within subfamilies are also observed in, for example, ABC transporters[32].

Our E2P crystal structure and MD simulations of LpCopA in combination with mutational analyses support a unique release mechanism for Cu^+ P_{IB}-type ATPases. The observed extracellular release pathway is likely to be involved in specific and controlled delivery to Cu^+-acceptor chaperones[33], thus preventing detrimental effects of free copper in the extracellular space, or to other cuproproteins that need the ion for function[34,35]. The pathway further explains why Menkes' and Wilson's mutations in this region impair the function of ATP7A and ATP7B. The high prevalence and critical function of P_{IB} genes in pathogenic bacteria for intraphagolysosomal copper defense[36,37] and the mutation sensitivity of the exit pathway point to a putative site for inhibitors with favorable access from the outside of the cells,

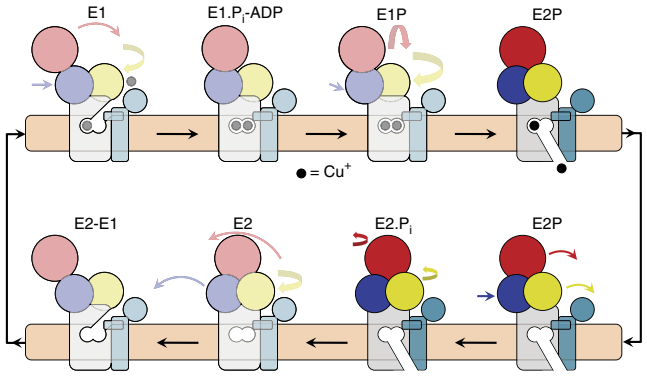

Figure 6 Mechanistic implications of the open E2.P_i state. The CopA domains are colored as in **Figure 1b**, with the known structures of the reaction cycle highlighted with bright colors. Colored arrows indicate the coming movements of the corresponding domains. In contrast to those of the well-characterized calcium P-type ATPase SERCA[16], no major movements are identified between the transmembrane domains of the E2P and E2.P_i LpCopA states, thus indicating a class-specific transport mechanism with an open release pathway associated with dephosphorylation.

similar to cardiotonic steroids and omeprazole, which are clinically used inhibitors of Na^+,K^+-ATPase and H^+,K^+-ATPase.

METHODS

Methods and any associated references are available in the online version of the paper.

Accession codes. Coordinates and structure factors for the E2P state of LpCopA (E2–BeF_3^-) have been deposited in the Protein Data Bank under accession code 4BBJ.

Note: Any Supplementary Information and Source Data files are available in the online version of the paper.

ACKNOWLEDGMENTS

We thank J.L. Karlsen for support on crystallographic computing. M.A. was supported in part by a Senior Postdoctoral Fellowship from the US National Science Foundation I2CAM International Materials Institute and a Marie Curie Career Integration Grant (FP7-MC-CIG-618558). The research was also supported by US National Institutes of Health grants GM074637 and GM086685 (S.H.W.). D.M. and O.S. were supported by the Graduate School of Science and Technology at Aarhus University. P.N. was supported by an advanced research grant (Biomemos) of the European Research Council. MD simulations were supported in part by the US National Science Foundation through TeraGrid (now Xsede) resources provided by the Texas Advanced Computing Center at the University of Texas at Austin.

AUTHOR CONTIBUTIONS

M.A. performed MD simulations; L.B.M. provided the *in vivo* strain and plasmid; D.M., O.S., T.K. and A.M.N. established DNA constructs; D.M. and O.S. performed the protein purifications; O.S. executed activity measurements; D.M. crystallized proteins, processed data and solved the crystal structures, guided by P.N. and P.G.; and all authors analyzed results. M.A. and P.G. designed the project, supervised by S.H.W. and P.N.; M.A., D.M., O.S. and P.G. generated figures; and all authors contributed to the writing of the paper.

COMPETING FINANCIAL INTERESTS

The authors declare no competing financial interests.

1. Lutsenko, S. & Kaplan, J.H. Organization of P-type ATPases: significance of structural diversity. *Biochemistry* **34**, 15607–15613 (1995).
2. Kühlbrandt, W. Biology, structure and mechanism of P-type ATPases. *Nat. Rev. Mol. Cell Biol.* **5**, 282–295 (2004).
3. Argüello, J.M., Eren, E. & Gonzalez-Guerrero, M. The structure and function of heavy metal transport P1B-ATPases. *Biometals* **20**, 233–248 (2007).
4. Vulpe, C., Levinson, B., Whitney, S., Packman, S. & Gitschier, J. Isolation of a candidate gene for Menkes disease and evidence that it encodes a copper-transporting ATPase. *Nat. Genet.* **3**, 7–13 (1993).
5. Bull, P.C., Thomas, G.R., Rommens, J.M., Forbes, J.R. & Cox, D.W. The Wilson disease gene is a putative copper transporting P-type ATPase similar to the Menkes gene. *Nat. Genet.* **5**, 327–337 (1993).
6. Albers, R.W. Biochemical aspects of active transport. *Annu. Rev. Biochem.* **36**, 727–756 (1967).
7. Post, R.L., Hegyvary, C. & Kume, S. Activation by adenosine triphosphate in the phosphorylation kinetics of sodium and potassium ion transport adenosine triphosphatase. *J. Biol. Chem.* **247**, 6530–6540 (1972).
8. Toyoshima, C., Nakasako, M., Nomura, H. & Ogawa, H. Crystal structure of the calcium pump of sarcoplasmic reticulum at 2.6 A resolution. *Nature* **405**, 647–655 (2000).
9. Toyoshima, C. & Nomura, H. Structural changes in the calcium pump accompanying the dissociation of calcium. *Nature* **418**, 605–611 (2002).
10. Sørensen, T.L., Moller, J.V. & Nissen, P. Phosphoryl transfer and calcium ion occlusion in the calcium pump. *Science* **304**, 1672–1675 (2004).
11. Toyoshima, C. & Mizutani, T. Crystal structure of the calcium pump with a bound ATP analogue. *Nature* **430**, 529–535 (2004).
12. Olesen, C., Sorensen, T.L., Nielsen, R.C., Moller, J.V. & Nissen, P. Dephosphorylation of the calcium pump coupled to counterion occlusion. *Science* **306**, 2251–2255 (2004).
13. Olesen, C. *et al.* The structural basis of calcium transport by the calcium pump. *Nature* **450**, 1036–1042 (2007).
14. Winther, A.M. *et al.* The sarcolipin-bound calcium pump stabilizes calcium sites exposed to the cytoplasm. *Nature* **495**, 265–269 (2013).
15. Toyoshima, C. *et al.* Crystal structures of the calcium pump and sarcolipin in the $Mg2^+$-bound E1 state. *Nature* **495**, 260–264 (2013).
16. Møller, J.V., Olesen, C., Winther, A.M. & Nissen, P. The sarcoplasmic Ca2+-ATPase: design of a perfect chemi-osmotic pump. *Q. Rev. Biophys.* **43**, 501–566 (2010).
17. Mattle, D. *et al.* On allosteric modulation of P-type Cu-ATPases. *J. Mol. Biol.* **425**, 2299–2308 (2013).
18. Gourdon, P. *et al.* Crystal structure of a copper-transporting PIB-type ATPase. *Nature* **475**, 59–64 (2011).
19. González-Guerrero, M., Eren, E., Rawat, S., Stemmler, T.L. & Arguello, J.M. Structure of the two transmembrane Cu^+ transport sites of the Cu^+-ATPases. *J. Biol. Chem.* **283**, 29753–29759 (2008).
20. Jardetzky, O. Simple allosteric model for membrane pumps. *Nature* **211**, 969–970 (1966).
21. Petrek, M. *et al.* CAVER: a new tool to explore routes from protein clefts, pockets and cavities. *BMC Bioinformatics* **7**, 316 (2006).
22. Shannon, R.D. Revised effective ionic-radii and systematic studies of interatomic distances in halides and chalcogenides. *Acta Crystallogr. A* **32**, 751–767 (1976).
23. Huang, Z. & Tajkhorshid, E. Identification of the third Na^+ site and the sequence of extracellular binding events in the glutamate transporter. *Biophys. J.* **99**, 1416–1425 (2010).
24. Renthal, R. Buried water molecules in helical transmembrane proteins. *Protein Sci.* **17**, 293–298 (2008).
25. Baginski, E.S., Foa, P.P. & Zak, B. Microdetermination of inorganic phosphate, phospholipids, and total phosphate in biologic materials. *Clin. Chem.* **13**, 326–332 (1967).
26. Gourdon, P., Sitsel, O., Karlsen, J.L., Moller, L.B. & Nissen, P. Structural models of the human copper P-type ATPases ATP7A and ATP7B. *Biol. Chem.* **393**, 205–216 (2012).
27. Barry, A.N. *et al.* The lumenal loop Met672-Pro707 of copper-transporting ATPase ATP7A binds metals and facilitates copper release from the intramembrane sites. *J. Biol. Chem.* **286**, 26585–26594 (2011).
28. Tadini-Buoninsegni, F. *et al.* ATP dependent charge movement in ATP7B Cu^+-ATPase is demonstrated by pre-steady state electrical measurements. *FEBS Lett.* **584**, 4619–4622 (2010).
29. Lewis, D. *et al.* Distinctive features of catalytic and transport mechanisms in mammalian Ca^{2+} (SERCA) and Cu^+ (ATP7A/B) ATPases. *J. Biol. Chem.* **278**, 32717–32727 (2012).
30. Hatori, Y. *et al.* Intermediate phosphorylation reactions in the mechanism of ATP utilization by the copper ATPase (CopA) of *Thermotoga maritima*. *J. Biol. Chem.* **283**, 22541–22549 (2008).
31. Poulsen, H. *et al.* Neurological disease mutations compromise a C-terminal ion pathway in the Na^+/K^+-ATPase. *Nature* **467**, 99–102 (2010).
32. Hollenstein, K., Dawson, R.J. & Locher, K.P. Structure and mechanism of ABC transporter proteins. *Curr. Opin. Struct. Biol.* **17**, 412–418 (2007).
33. Raimunda, D., Gonzalez-Guerrero, M., Leeber, B.W. III & Arguello, J.M. The transport mechanism of bacterial Cu^+-ATPases: distinct efflux rates adapted to different function. *Biometals* **24**, 467–475 (2011).
34. Waldron, K.J. *et al.* Structure and metal loading of a soluble periplasm cuproprotein. *J. Biol. Chem.* **285**, 32504–32511 (2010).
35. Hassani, B.K., Astier, C., Nitschke, W. & Ouchane, S. CtpA, a copper-translocating P-type ATPase involved in the biogenesis of multiple copper-requiring enzymes. *J. Biol. Chem.* **285**, 19330–19337 (2010).
36. Ward, S.K., Abomoelak, B., Hoye, E.A., Steinberg, H. & Talaat, A.M. CtpV: a putative copper exporter required for full virulence of *Mycobacterium tuberculosis*. *Mol. Microbiol.* **77**, 1096–1110 (2010).
37. Festa, R.A. & Thiele, D.J. Copper at the front line of the host-pathogen battle. *PLoS Pathog.* **8**, e1002887 (2012).
38. Hub, J.S., de Groot, B.L. & van der Spoel, D. g_wham: a free weighted histogram analysis implementation including robust error and autocorrelation estimates. *J. Chem. Theory Comput.* **6**, 3713–3720 (2010).

ONLINE METHODS

Sample preparation. LpCopA mutants were generated with Agilent Technologies' QuikChange Lightning site-directed-mutagenesis kit with the full-length non-tagged *lpg1024* gene in pET22b(+) (Novagen). Cell growth to solubilization, in the detergent $C_{12}E_8$ (octaethylene glycol monododecyl ether), and ultracentrifugation were conducted as described previously[18]. For crystallization, the sample was further purified according to this protocol, whereas each construct for *in vitro* characterization was loaded onto a separate pre-equilibrated 5-ml affinity column, either GE Healthcare HisTrap HP or Qiagen Ni-NTA Superflow Cartridge, washed with 20 mM Tris-HCl, pH 7.6, 200 mM KCl, 1 mM $MgCl_2$, 20% glycerol, 5 mM β-mercaptoethanol (BME) and 0.28 mM $C_{12}E_8$, and eluted with 500 mM imidazole. The buffer of the concentrated protein was thereafter exchanged with a GE Healthcare HiTrap Desalting column to 20 mM MOPS-KOH, pH 6.8, 80 mM KCl, 1 mM $MgCl_2$, 20% glycerol, 5 mM BME and 0.28 mM $C_{12}E_8$. The constructs were concentrated and the purity estimated with SDS-PAGE. To assess relative protein concentrations, the intensity of individual LpCopA bands at ~75 kDa were quantified with ImageJ[39]. A second SDS-PAGE gel (**Supplementary Fig. 4a**) was generated with equal protein amounts, as calculated from the first gel. The protein concentration of the D426N mutant was determined with light absorbance at 280 nm and used as reference in the activity assay (described below).

***In vitro* characterization.** The Baginski method with arsenic detection under aerated conditions was used to assess ATPase activity[25]. Measurements were conducted with equal amounts of protein for each construct as judged by ImageJ (and shown in **Supplementary Fig. 4a**), corresponding to 3.8 μM for D426N, 40 mM MOPS-KOH, pH 6.8, 150 mM NaCl, 5 mM KCl, 5 mM $MgCl_2$, 20 mM $(NH4)_2SO_4$, 20 mM L-cysteine, 5 mM NaN_3, 0.25 mM Na_2MoO_4, 1.2 mg/ml L-α-phosphatidylcholine lipids from soybean and 3.7 mM $C_{12}E_8$ in a total volume of 50 μl. 10 μM ammonium tetrathiomolybdate was added to prevent activity from background copper contaminants, and the protein was incubated for 15 min with 1 mM $CuCl_2$ (reduced to Cu^+). Reactions were started by addition of 4.8 mM ATP, incubated at 37 °C with shaking for 25 min and stopped by addition of 50 μL of freshly made stop solution (0.083% SDS, 417 mM HCl, 142 mM L-ascorbic acid and 4.72 mM $(NH_4)_6Mo_7O_{24}•4H_2O$). After 10 min of incubation at 19 °C, 75 μL stabilizing solution (154 mM $NaAsO_2$, 68 mM $Na_3C_6H_5O_7•2H_2O$ and 349.4 mM CH_3COOH) was added and incubated for 30 min at 19 °C. Absorbance was measured at 860 nm with a PerkinElmer VICTOR3 multilabel plate counter. The raw output data (**Supplementary Table 1a**) were thereafter scaled (**Supplementary Table 1b**) to account for the subtle variations in the relative intensities of **Supplementary Figure 4a**. These data were then plotted on a scale of 100% (wild-type LpCopA activity) to 0% (D426N mutant activity), through removal of the background of the D426N dead mutant (**Fig. 4c**). One experiment with nine replicates was done for the *in vitro* activity data. To assess the reproducibility of our assay, two mutations were tested with an additional independent experiment (**Supplementary Fig. 4d**).

***In vivo* characterization.** The *E. coli* CopA-deleted strain CN2328, its progenitor strain CN1709 and the plasmid pCN2345 containing the native *E. coli* CopA promoter used here have been described previously[40]. pCN2345 was mutated to allow replacement of *E. coli* CopA with LpCopA with maintained promoter and wild-type and mutant LpCopA incorporated separately. The plasmids were then transformed into CN2328, and an empty pET22b(+) vector was transformed into CN1709 cells and used as a control. Precultures were grown overnight and their OD_{600nm} adjusted to 1.0 before inoculation. 10 μl of cells were used to inoculate 190 μl of LB medium with 100 μg/ml ampicillin, and $CuCl_2$ concentrations were adjusted to 0 and 3 mM. The inoculated media were grown in 96-well plates in a shaking incubator at 37 °C, and OD_{560nm} was measured in hourly intervals with a PerkinElmer VICTOR3 multilabel plate counter. (The growth curves of the cells at different $CuCl_2$ concentrations are shown in **Supplementary Fig. 4b**,**c**, and the final time point for 3 mM $CuCl_2$ is shown in **Fig. 4c**.) Three independent experiments were conducted, with 3 replicates each for the first and third experiments, and 15 replicates for the second experiment. The averaged value of the averages for each mutant in every independent experiment at the final time point for 3 mM $CuCl_2$ was used in **Figure 4c**, and wild-type LpCopA activity was set as 100%. Error bars were calculated by three data points per mutant per experiment. The three data points of the second experiment were selected by taking the lowest, highest and most average value for each mutant from the 15 replicates. M100L was not cloned for the *in vivo* assay.

Crystallization, data collection and model building. Crystallization of the LpCopA E2–BeF_3^- complex was performed by hanging-drop vapor diffusion. 0.15 ml 10 mg/ml LpCopA was relipidated for 16 h according to the HiLiDe method[41] with 0.5 mg DOPC and between 5 μl and 12 μl 100 mg/ml $C_{12}E_8$. The sample was centrifuged for 10 min at 100,000*g* and incubated with 10 mM NaF, 3.2 mM EGTA, 10 μM ammonium tetrathiomolybdate (TTM) and 2 mM $BeSO_4$. The best crystals (in the space group *C*2) were found after two days with 5 mM β-NAD in the protein solution and a precipitant solution containing 10% glycerol, 200 mM KCl, 3% *t*-BuOH, 14% PEG 2K MME and 5 mM BME mixed 1:1 with the protein solution. The $P2_12_12_1$ crystal form, displaying a different packing, grew by addition of 36.7 mM Fos-choline-10 to the protein solution. Screening of diffraction properties was conducted at Maxlab, SLS and ESRF, and final data were collected at ID29 at ESRF with a wavelength of 0.9763 Å, a temperature of 100 K and a pixel detector (Pilatus 6M) and scaled with XDS[42]. Initial phases were obtained by molecular replacement with Phaser[43] with the E2–AlF_4^- structure of LpCopA (PDB 3RFU[18]) as a search model. Iterative refinement and model building were performed with Phenix[44] and the molecular graphics program Coot[45]. The low-resolution E2–BeF_3^- structure ($P2_12_12_1$ crystal form) was determined with Phaser with the above high-resolution structure as a search model (PDB 4BBJ) and subjected to rigid-body refinement in Phenix[44]. Structures were analyzed with MolProbity, which indicated that 96.2, 3.0 and 0.8% of the residues were in the favored, allowed and nonfavored regions, respectively, for the high-resolution structure (in space group *C*2).

Building the MD systems. For the E2.P_i state (based on the E2–AlF_4^- structure, PDB 3RFU[18], chain A) and E2P state (E2–BeF_3^-, PDB 4BBJ), proteins with ligands were inserted into the lipid bilayer by alignment of the centers of mass of the TM region and a 500-molecule DOPC bilayer (built with the CHARMM-GUI membrane builder[46]) and solvated in excess water. Alternative docking methods resulted in similar insertion depths (data not shown)[47,48]. Electric neutrality was achieved by addition of seven and nine Na^+ counterions to the E2.P_i and E2P system, respectively. The E2.P_i P94A and P710A mutants, generated with the VMD plugin psfgen[49], were constructed in a similar fashion.

MD simulation. After a 10,000-step conjugate-gradient energy minimization and gradual heating from 0 to 310 K over 120 ps, two consecutive 1-ns simulations at constant temperature (310 K) and volume (NVT ensemble) equilibrated lipids and water molecules, respectively. The protein was then progressively released from its initial configuration over seven 1-ns simulations, and this was followed by a production run at constant temperature (310 K) and pressure (1 atm) (NPT ensemble). The production runs for the wild-type, P94A and P710A E2.P_i states were 100 ns, and for the E2P state was 85 ns. Molecular dynamics simulations were run with the NAMD 2.7 package[50]. The CHARMM22 including CMAP correction and CHARMM36 force fields[51,52] were used for protein and lipids, respectively, and the TIP3P model was used for the water molecules[53]. A time step of 1 fs was used to integrate the equations of motion, and a reversible multiple-time-step algorithm[54] of 4 fs was used for the electrostatic forces and 2 fs for short-range, nonbonded forces. The smooth particle mesh Ewald method[55,56] was used to calculate electrostatic interactions. The short-range interactions were cut off at 12 Å. All bond lengths involving hydrogen atoms were held fixed with the SHAKE[57] and SETTLE[58] algorithms. A Langevin dynamics scheme was used for thermostating, and Nosé–Hoover–Langevin pistons were used for pressure control[59,60]. Molecular graphics and simulation analyses were generated with the VMD 1.8.7 package[49]. The evolution of the simulation cell dimensions shows the simulations to equilibrate within 20 ns (**Supplementary Fig. 3a**,**b**). The r.m.s. deviation for the E2.P_i-state simulations were relatively high (>4 Å), whereas the E2P state was less flexible, with an r.m.s. deviation of ~2 Å (**Supplementary Fig. 3c**,**d**). The relatively high values of r.m.s. deviations for the E2.P_i-state simulations stemmed from the large soluble headpiece because the TM domain displayed substantial stability, reaching a plateau at ~2 Å after 20 ns. To account for the underlying structural factors for the large r.m.s. deviation, we measured the evolution of the centers of mass (COM) for the A/N/P domains (**Supplementary Fig. 3e**). We note substantial COM stability in all dimensions for the individual

domains and conclude that the large r.m.s. deviation stems from inherent flexibility of the domains and loop regions rather than from rigid-body motions.

MD simulation with Cu^+. To describe the energy barriers involved in transport of Cu^+ along the water-filled pathway, the potential of mean force (PMF) was calculated with GROMACS 4.6.3 (ref. 61) and the ffGromos53a6 force field[62], which contains Cu^+ parameters. The last frame of the CHARMM E2.P_i simulation was formatted according to the Gromos force field, and a Cu^+ ion was placed between ion-coordinating residues Cys382 and Met717. The DOPC lipids and water molecules were described by parameters derived from the ffGromos53a6 force field[63] and the simple point charge (SPC) water model[64], respectively. The system was first energy-minimized according to a steepest descent algorithm for 5,000 steps. The GROMACS pull code was used to generate configurations for the umbrella sampling with a 1,000 kJ mol^{-1} nm^{-2} force constant applied on Cu^+ in the *z* dimension directed toward the extracellular side. A pull rate of 2.5 Å/ns was applied for 10 ns. The Cα atoms of six remote residues (111, 115, 169, 367, 706 and 709) were restrained to keep the system from drifting when applying the force. A 2-fs time step was used, and short-range nonbonded interactions were cut off at 1.4 nm, with long-range electrostatics calculated with the particle mesh Ewald (PME) algorithm[55,56]. The temperature of the system was maintained by independent coupling of the protein and nonprotein atoms to an external temperature bath at 310 K with a Nose–Hoover thermostat[65,66], and the Parrinello–Rahman barostat[67,68] was used to isotropically regulate pressure. The length of all bonds within the protein was constrained with the LINCS algorithm[69]. Snapshots spaced by 1 Å were taken from the pulling simulation to generate the starting configurations for the umbrella-sampling windows. Each window was equilibrated for 100 ps and was followed by 5 ns of umbrella sampling and then extraction of the PMF with the weighted histogram analysis method[70], implemented in the GROMACS package[38]. Statistical errors were quantified by bootstrap analysis.

Figures. **Figures 1c**,**d**, **4a**,**b** and **5** in the main text were made with VMD[49], and **Figures 2**, **3a**,**b** and **4d** were done with PyMOL (http://www.pymol.org/).

39. Schneider, C.A., Rasband, W.S. & Eliceiri, K.W. NIH Image to ImageJ: 25 years of image analysis. *Nat. Methods* **9**, 671–675 (2012).
40. Petersen, C. & Moller, L.B. Control of copper homeostasis in *Escherichia coli* by a P-type ATPase, CopA, and a MerR-like transcriptional activator, CopR. *Gene* **261**, 289–298 (2000).
41. Gourdon, P. *et al.* HiLiDe: systematic approach to membrane protein crystallization in lipid and detergent. *Cryst. Growth Des.* **11**, 2098–2106 (2011).
42. Kabsch, W. Automatic processing of rotation diffraction data from crystals of initially unknown symmetry and cell constants. *J. Appl. Crystallogr.* **26**, 795–800 (1993).
43. McCoy, A.J. *et al.* Phaser crystallographic software. *J. Appl. Crystallogr.* **40**, 658–674 (2007).
44. Adams, P.D. *et al.* PHENIX: a comprehensive Python-based system for macromolecular structure solution. *Acta Crystallogr. D Biol. Crystallogr.* **66**, 213–221 (2010).
45. Emsley, P. & Cowtan, K. Coot: model-building tools for molecular graphics. *Acta Crystallogr. D Biol. Crystallogr.* **60**, 2126–2132 (2004).
46. Jo, S., Lim, J.B., Klauda, J.B. & Im, W. CHARMM-GUI membrane builder for mixed bilayers and its application to yeast membranes. *Biophys. J.* **97**, 50–58 (2009).
47. Sansom, M.S., Scott, K.A. & Bond, P.J. Coarse-grained simulation: a high-throughput computational approach to membrane proteins. *Biochem. Soc. Trans.* **36**, 27–32 (2008).
48. Lomize, M.A., Lomize, A.L., Pogozheva, I.D. & Mosberg, H.I. OPM: orientations of proteins in membranes database. *Bioinformatics* **22**, 623–625 (2006).
49. Humphrey, W., Dalke, A. & Schulten, K. VMD: visual molecular dynamics. *J. Mol. Graph.* **14**, 33–38 (1996).
50. Phillips, J.C. *et al.* Scalable molecular dynamics with NAMD. *J. Comput. Chem.* **26**, 1781–1802 (2005).
51. Klauda, J.B. *et al.* Update of the CHARMM all-atom additive force field for lipids: validation on six lipid types. *J. Phys. Chem. B* **114**, 7830–7843 (2010).
52. Mackerell, A.D., Feig, M. & Brooks, C.L. Extending the treatment of backbone energetics in protein force fields: Limitations of gas-phase quantum mechanics in reproducing protein conformational distributions in molecular dynamics simulations. *J. Comput. Chem.* **25**, 1400–1415 (2004).
53. Jorgensen, W.L., Chandrasekhar, J., Madura, J.D., Impey, R.W. & Klein, M.L. Comparison of simple potential functions for simulating liquid water. *J. Chem. Phys.* **79**, 926–935 (1983).
54. Grubmüller, H., Heller, H., Windemuth, A. & Schulten, K. Generalized verlet algorithm for efficient molecular dynamics simulations with long-range interactions. *Mol. Simul.* **6**, 121–142 (1991).
55. Darden, T., York, D. & Pedersen, L. Particle mesh Ewald: an *n*.log(*n*) method for Ewald sums in large systems. *J. Chem. Phys.* **98**, 10089–10092 (1993).
56. Essmann, U. *et al.* A smooth particle mesh Ewald method. *J. Chem. Phys.* **103**, 8577–8593 (1995).
57. Ryckaert, J.P., Ciccotti, G. & Berendsen, H.J.C. Numerical-integration of cartesian equations of motion of a system with constraints: molecular-dynamics of N-alkanes. *J. Comput. Phys.* **23**, 327–341 (1977).
58. Miyamoto, S. & Kollman, P.A. Settle: an analytical version of the shake and rattle algorithm for rigid water models. *J. Comput. Chem.* **13**, 952–962 (1992).
59. Feller, S.E., Zhang, Y.H., Pastor, R.W. & Brooks, B.R. Constant-pressure molecular-dynamics simulation: the Langevin piston method. *J. Chem. Phys.* **103**, 4613–4621 (1995).
60. Martyna, G.J., Tobias, D.J. & Klein, M.L. Constant-pressure molecular-dynamics algorithms. *J. Chem. Phys.* **101**, 4177–4189 (1994).
61. Hess, B., Kutzner, C., van der Spoel, D. & Lindahl, E. GROMACS 4: algorithms for highly efficient, load-balanced, and scalable molecular simulation. *J. Chem. Theory Comput.* **4**, 435–447 (2008).
62. Oostenbrink, C., Villa, A., Mark, A.E. & van Gunsteren, W.F. A biomolecular force field based on the free enthalpy of hydration and solvation: the GROMOS force-field parameter sets 53A5 and 53A6. *J. Comput. Chem.* **25**, 1656–1676 (2004).
63. Poger, D., Van Gunsteren, W.F. & Mark, A.E. A new force field for simulating phosphatidylcholine bilayers. *J. Comput. Chem.* **31**, 1117–1125 (2010).
64. Berendsen, H.J.C., Postma, J.P.M., van Gunsteren, W.F. & Hermans, J. in *Intermolecular Forces* (ed. Pullman, B.) (Reidel, Dordrecht, 1981).
65. Hoover, W.G. Canonical dynamics: equilibrium phase-space distributions. *Phys. Rev. A* **31**, 1695–1697 (1985).
66. Nose, S. A unified formulation of the constant temperature molecular-dynamics methods. *J. Chem. Phys.* **81**, 511–519 (1984).
67. Nose, S. & Klein, M.L. Constant pressure molecular-dynamics for molecular-systems. *Mol. Phys.* **50**, 1055–1076 (1983).
68. Parrinello, M. & Rahman, A. Polymorphic transitions in single-crystals: a new molecular-dynamics method. *J. Appl. Phys.* **52**, 7182–7190 (1981).
69. Hess, B., Bekker, H., Berendsen, H.J.C. & Fraaije, J.G.E.M. LINCS: a linear constraint solver for molecular simulations. *J. Comput. Chem.* **18**, 1463–1472 (1997).
70. Kumar, S., Bouzida, D., Swendsen, R.H., Kollman, P.A. & Rosenberg, J.M. The weighted histogram analysis method for free-energy calculations on biomolecules: 1. The method. *J. Comput. Chem.* **13**, 1011–1021 (1992).

doi:10.1038/nsmb.2721